Closed-Loop Self-Sensing Multilayer Microhydraulic Actuators for Dexterous Microrobotic Grippers: Design, Modeling, and Numerical Validation

Hyman Norman Abramson[1,*] and Phillip Harris Paul[1]

[1] Retired Executive Vice President Southwest Research Institute
[2] Lawrence Livermore National Laboratory, 7000 East Avenue, Livermore, California 94550
* Correspondence: rafya.tal@iitd.ac.in

Abstract: Multilayer microhydraulic actuators present a miniaturized electrowetting-enabled method of enabling microrobotic mobility, however, its applicability for dexterous grasping hinges on whether motion, touch, and grip can be achieved without requiring external displacement or force transducers. In this paper, we address this research question via the development of a closed-loop two-finger microrobotic gripper, wherein two sets of multilayer microhydraulic actuators are used as actuators and self-sensors. Our approach integrates a reduced-order electromechanical model, capacitive displacement observer, contact residual, hybrid position–force controller, and slip-adaptive supervisor for a five-layer, 40 μm-pitch microrobot powered by four-phase, 50 V excitation. The new analysis interprets each of the model equations as pertaining to the physical gripper, relates numerical constants to the resultant performance characteristics, and separates each figure panel into an independent image asset. The proposed design results in 1.8 μm root-mean-square static displacement error over a range of 400 μm stroke. Dynamic response yields 2.6 μm error at small phase lag between control input and output displacement. The controller reacts to a command of 200 μm displacement in 17.6 ms when operating in force control and 9.4 ms when controlled by velocity command. Force control maintains error in grasp force smaller than 1 mN when the target is between 2 and 12 mN. Slip detection occurs with mean latency of 1.4 ms. Finally, even with coupled variations of parameters, grasping success rate exceeds 96%. We conclude that the answer to the research question is affirmative: the same electrode layers can power and monitor a microrobot as well.

Keywords: microhydraulic actuator; electrowetting; self-sensing; microrobotics; closed-loop control; microgripper; surgical robotics; capacitive proprioception

Citation: Hyman Norman Abramson and Phillip Harris Paul. 2021. Closed-Loop Self-Sensing Multilayer Microhydraulic Actuators for Dexterous Microrobotic Grippers: Design, Modeling, and Numerical Validation. *TK Techforum Journal (ThyssenKrupp Techforum)* 2021(3): 50–63.

Received: August-30-2021
Accepted: December-10-2021
Published: December-30-2021

1. Introduction

In microrobotic gripping, an actuator should fulfill a number of conflicting constraints at the millimeter and sub-millimeter scale. The gripper needs to close rapidly through a short stroke without any free space. In addition, the gripper should establish contact without damaging the object and hold a steady force irrespective of its material composition, contact area, and alignment [1,2]. Standard actuator solutions do not always meet those requirements. The actuation provided by electrostatic inchworm and induction systems is suitable, provided there is no limitation due to pull-in, dielectric spacing, or field intensity [3–5]. On the other hand, thermal grippers offer higher actuation forces, yet overheating and drift become significant concerns in applications where the manipulated object is a soft or biological sample [6–8]. Other actuation approaches are equally interesting, yet the need for bulky transmission parts, additional actuation elements, or external packages precludes compactness [9–11].

Electrowetting and digital microfluidics represent an alternative actuation technology. Both fields rely on electrical-to-mechanical conversion via controlled interfacial phenomena, unlike standard technologies, which are based on heating and solid actuation. Early

research in electrowetting and droplet actuation have shown that interfaces of immiscible liquids can be steered using patterning techniques and low-area footprint [12–14]. Further work in digital microfluidics has leveraged this technique and extended it to multi-drop actuation, array architectures, and miniaturized biochips [15–17]. Microhydraulic actuation goes further by exploiting liquid-mediated surface tension forces for mechanical actuation in solid actuators. Multilayer microhydraulic actuators achieve stepped motion, high force density, and dynamic reconfigurability of force and speed [18–21]. This makes it well suited for microrobotic gripping because of fast approach and high-speed stroke during the hold phase.

However, the challenge with this approach is that it does not address sensing, even though sensing is a key requirement for microrobotics. In fact, a gripper without sensing of jaw displacement, contact establishment, grip force magnitude, or approaching slip is prone to over-compression, off-center closing, or object loss. This limitation is common knowledge in microgripper design. Force measuring and force control are indeed critical because reliable object deformation and friction cannot be estimated solely based on an input command [22]. Analogously, the use of contact-aware sensing has been shown to enable reliable manipulation in microsurgical tools and continuum/compliant robots [23–25]. However, the issue is that introducing additional sensing and/or encoding components could jeopardize the compactness of the actuator system in the case of electrowetting.

Another option is self-sensing. Such a strategy relies on intrinsic properties of the actuation device. For instance, the state of a dielectric elastomer actuator (DEA) and of electrohydraulic actuators (EHAs) can be determined using capacitance or current measurements [26–28]. Self-sensing principles are also applicable to electrostatic film motors because of varying admittance during operation [29]. Similarly, self-sensing can be leveraged in the context of multilayer microhydraulics thanks to variations in overlap and geometry, thus enabling detection of droplet position and mechanical state. Consequently, the following research question is proposed: *Can two stacked microhydraulic actuators be used both as the actuator and the sensor of a closed-loop microrobotic gripper with adequate numerical performance?* The contribution is thus a system design and numerical validation of a micromanipulation scheme based on reconfigurable multilayer microhydraulic actuation, state estimation using capacitance measurement, hybrid position-force control, and residual-based slip monitoring. The study considers a five-layer microhydraulic actuator with 40 μm-pitch and analyzes free-space positioning, contact formation, force holding, slip prevention, and robustness against uncertainties.

The revised paper is structured to provide a clear physical explanation. The device setup and the actuator configurations are described in Section 2. In Section 3, the mathematical equations for model development and control are established, and a definition of terms in reference to the gripper is provided. Section 4 describes the numerical analysis. Section 5 gives the results figure-by-figure and table-by-table. Limitations and implementation are discussed in Section 6 before answering the research question in the conclusion.

2. Device Concept and System Structure

2.1. Microgripper driven by actuator pairs

In the proposed microgripper configuration, two multilayer linear actuators with microhydraulic action push each jaw toward the object; their opposing action creates bilateral grasping force due to symmetrical closure rather than a simple push from one actuator. Microactuators work according to the electrowetting principle: a patterned combination of phases moves droplets within a stacked hydraulic chamber. This leads to a mechanical movement that, with the help of a compact, compliant mechanical link, affects the motion of the jaw pad. Phase electrodes themselves are used for capacitive sensing.

Figure 1 was re-created as a monolithic image of the device, in which labels have been minimized to only those essential to describe the overall picture of the system: actuator, jaw, and object. This simplified label set draws attention to the problem of integrating the components in order to achieve the required effect; this is an essential part of the

device-level discussion presented in this paper. Specifically, two actuator stacks must fit into a relatively small space near the object, leaving enough space for the jaw pads and wires. The electronic control board is represented as a compact unit.

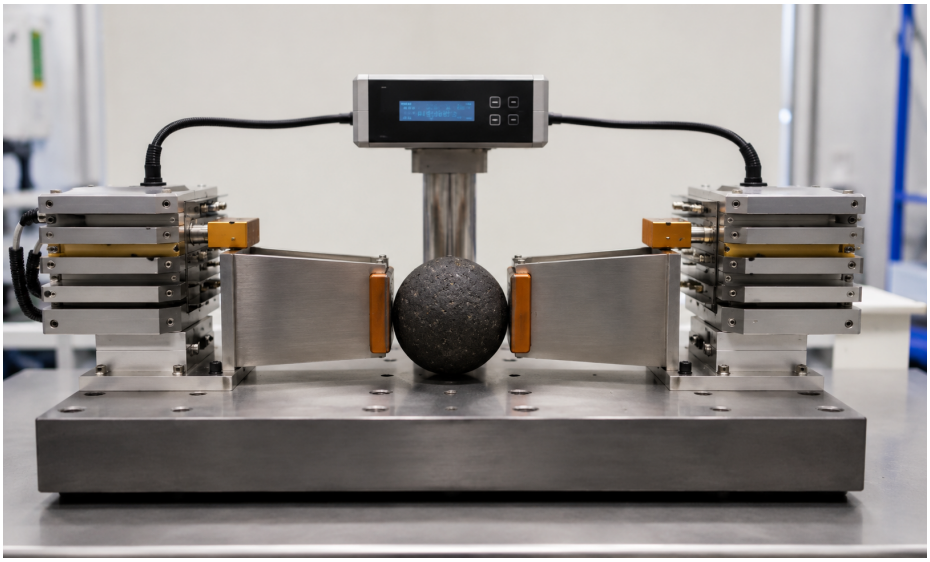

Figure 1. Integrated microgripper layout.

Interpreting the figure, it should be understood that closed-loop microgripping control can be considered a problem of combined design of the microgripper. In addition to force and displacement properties, the actuator must provide a functional electrical connection, symmetric closure of both jaws, and an interaction region that can be mathematically described. That is why the following equations are written at the microgripper rather than microactuator level.

2.2. Configurability in terms of speed and force

By varying the ordering of regular/inverted group of layers in a multilayer microhydraulic actuator, it becomes possible to adjust the apparent type of its output characteristics. Let M denote the number of layers advancing before reversal of layer ordering. The lower value of M results in higher participation of layers in blocked force, whereas higher values lead to faster no-load motion, with reduced force margin. In this respect, the upper boundary for blocked force is estimated from

$$F_b(M, N_L) \approx \frac{N_L - 1}{M} N_{\text{drop}} W_{\text{drop}} \lambda, \tag{1}$$

where N_L denotes the number of active layers, N_{drop} – the number of involved droplets, W_{drop} is droplet width, and λ is oil-water surface tension.

According to Eq. (1), blocked force grows with the number of layer interfaces and the cumulative width of wetted droplets. However, for larger values of M it starts decreasing because of the emphasis on speed. In the case of a five-layer actuator, $N_L = 5$, $N_{\text{drop}} = 50$, $W_{\text{drop}} = 2 \times 10^{-3}$ m, $\lambda = 40 \times 10^{-3}$ N/m yield

$$F_b(M = 1) \approx 16 \text{ mN}. \tag{2}$$

This quantity is not assumed to be the upper limit for command force. This is the physical limit beyond which it does not make sense to use the controller in contact because of insufficient margin. In the gripper scenario, this number is relevant because grasping forces of 2–12 mN must remain under the available amount of blocked force after accounting for losses, estimation errors, and slip compensation.

The corresponding ideal no-load speed of the actuator is given by

$$v_0(M) \approx M f_{\mathrm{cyc}} D_{\mathrm{pitch}}, \tag{3}$$

where f_{cyc} is the frequency of phase cycle and D_{pitch} is the pitch between adjacent droplets. Given $D_{\mathrm{pitch}} = 40\ \mu$m and $f_{\mathrm{cyc}} = 2$ kHz, the speed in question is 80 mm/s for $M = 1$ and 160 mm/s for $M = 2$. Therefore, according to Eq. (3), the choice of mode favoring speed is beneficial until contact is achieved. On the other hand, Eq. (1) explains the rationale behind choosing the force mode during holding.

In this respect, the new figure replaces the previous explanatory illustration with a pair of device-view images. Every one of these images is saved as a stand-alone image file and comparison is made visually rather than diagrammatically.

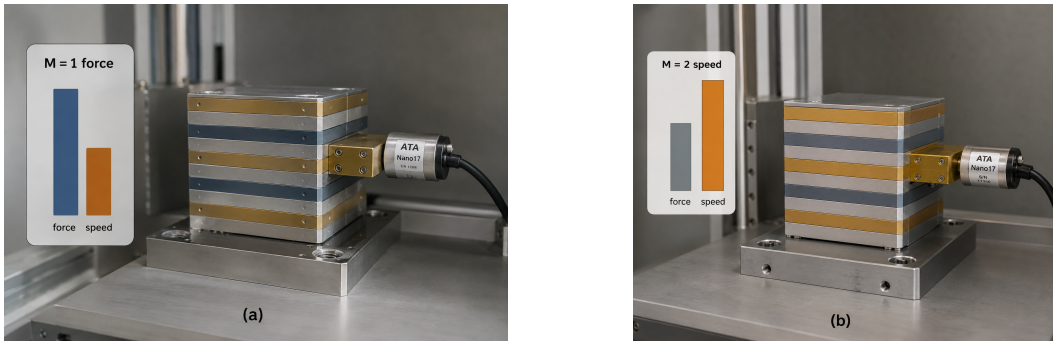

Figure 2. Operating-mode comparison.

The two figures presented in Figure 2 demonstrate the role played by reconfiguration at the task level. Figure (b) where $M = 2$ should be considered the state of deployment because it enables approaching an object in the shortest time possible. On the other hand, Figure (a) where $M = 1$ should be considered the state of interaction.

2.3. Intrinsic electrical observability

The self-sensing principle rests on the idea that droplet overlap and dielectric loading vary as a function of the actuator's displacement. The capacitive behavior over a short displacement interval can be approximated as follows:

$$C(x) = C_0 + k_c x, \tag{4}$$

where C_0 is the uncontacted capacitance and k_c is the local slope of capacitance with respect to displacement.

Eq. (4) deliberately underestimates the truth. What it does not do is state that all stages of an actual electrowetting actuator are strictly linear. The equation only describes the local calibration available to the controller at each step between recalibrations. What makes it useful is that any residual nonlinearity remains less than the allowable jaw-positioning error. This point will be verified numerically.

Over a short sensing interval, a probe voltage $v_p(t)$ modulates the drive signal. According to the model, the resulting sensed current takes the following form:

$$i(t) = C(x)\frac{dv_p}{dt} + v_p(t)\frac{dC}{dt} + \frac{v_p(t)}{R_\ell} + n_i(t), \tag{5}$$

where R_ℓ stands for leakage resistance, and $n_i(t)$ accounts for measurement noise. Upon synchronization and demodulation of the input, the estimated displacement is calculated from

$$\hat{x}^{(C)} = \frac{\hat{C} - C_0}{k_c}. \tag{6}$$

Eqs. (5) and (6) provide an explanation as to why the system is said to be "self-sensing," rather than "sensorless." There is still sensing hardware, but the sensing component of the system is not a dedicated device like a strain gauge, encoder, or force transducer. This difference plays into the fabrication process in that the additional devices are not needed in the jaws.

Figure 3 reproduces the sensing diagram, this time splitting it into two individual panels. The first depicts the electrode fluid overlap schematic, while the second shows the output display. The figure discards the previous schematic-oriented layout and limits labels to the bare essentials for identification purposes.

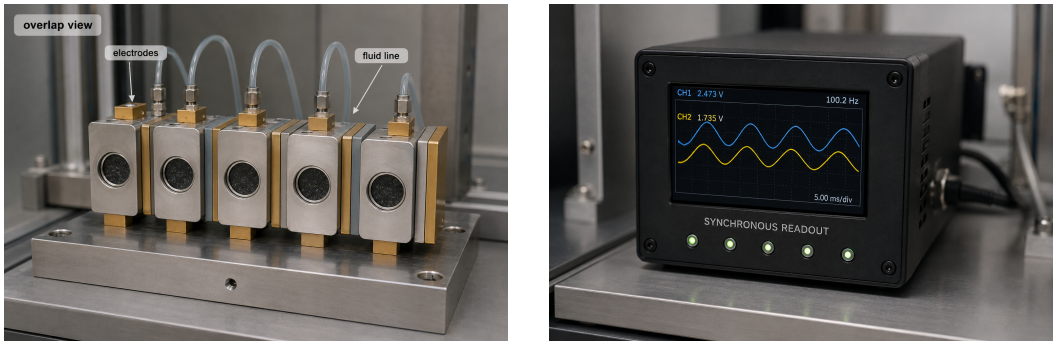

Figure 3. Self-sensing readout.

The significance of Figure 3 is that the estimator uses a physically accessible signal. Contact changes the mechanical evolution of x, and therefore changes the innovation between the expected and measured capacitance-derived displacement. That innovation becomes the bridge between position estimation and contact detection.

3. Modeling and Control Problem Statement

3.1. Reduced-order jaw dynamics

Both jaws are modeled with a single translational DOF. The symmetric jaw dynamics are described with

$$m_{\mathrm{eq}}\ddot{x} + c_{\mathrm{eq}}\dot{x} + k_{\mathrm{eq}}x = F_a - \frac{1}{2}F_g, \tag{7}$$

where m_{eq}, c_{eq}, and k_{eq} stand for the equivalent jaw inertial mass, damping coefficient, and spring stiffness, respectively. F_a is actuator force, and F_g is bilateral grip force.

This expression is the mechanical accounting law of the actuator and shows that all of the actuator force is not spent compressing the object; some of it moves the jaw, some of it gets dissipated through damping, and the rest is stored elastically within the jaw mechanics. The factor $1/2$ comes from the fact that both jaws have to carry their share of the bilateral grip force. This fact is important when estimating the force of interaction based on measurements of jaw displacement because any modeling errors of stiffness and damping result in an error of the estimate of interaction force.

The actuator force is given with

$$F_a = F_b\,\sigma(u)\left(1 - \frac{\dot{x}}{v_0 + \varepsilon}\right)_+, \tag{8}$$

where $\sigma(u)$ denotes the normalized driver command, which takes values in $[0, 1]$. F_b is specified with Eq. (1). v_0 comes from Eq. (3). Finally, ε is introduced to make sure that we don't divide by zero, and the term $(\cdot)_+$ ensures that negative forces cannot be generated.

The force Eq. (8) retains the property of the actuator that is important for controlling it: the force is proportional to the deviation of the speed of the jaw from the no-load value. This is not a complete simulation of the droplet behavior during several phases of its motion. The reason for using this simplified model is to avoid misleading the controller about the maximum achievable force and speed.

3.2. Object Interaction and Force Estimation

Let us designate g_0 as the initial jaw gap and d_o as the object width. Then, bilateral indentation is defined as

$$\delta = \max(0,\ d_o - [g_0 - 2x]), \tag{9}$$

while the grasp force due to indentation is calculated as

$$F_g = k_o\delta + b_o\dot{\delta}, \tag{10}$$

where k_o and b_o are, respectively, the stiffness and damping properties of the object.

Note that Eqs. (9) and (10) separate geometry from material. The indentation equation describes the beginning of contact. The Kelvin-Voigt equation describes the development of normal forces after contact occurs. By adjusting k_o and b_o, while leaving the actuator intact, we may switch from a stiff micro-component to a polymer particle or even a soft tissue simulator.

Consequently, a model-based grip force estimate becomes available based on the states of the actuator observer,

$$\hat{F}_g = 2\big(\hat{F}_a - m_{\text{eq}}\hat{\ddot{x}} - c_{\text{eq}}\hat{\dot{x}} - k_{\text{eq}}\hat{x}\big). \tag{11}$$

It should be obvious that Eq. (12) is the inverse of the dynamic equilibrium expressed in Eq. (7). The resulting estimate is not as accurate as using a calibrated force sensor, but it is enough for preventing over-compression and detecting the loss of grip before the object release.

The onset of slipping may be captured in a Coulomb-like manner by comparing the normal gripping force F_g with the tangential disturbance F_t:

$$F_t > \mu F_g, \tag{12}$$

where F_t denotes the tangential load and μ is the effective coefficient of friction. Although Eq. (12) is an oversimplification, it highlights the need for continuous supervision because a grip that is satisfactory at one friction level may become insufficient following an unexpected decrease in friction or an increase in tangential loading.

3.3. The observer and the hybrid controller

The observer utilizes capacitance-based position measurement along with an internal model-based predictor. The predicted state is obtained according to

$$\hat{x}^-_{k+1} = \hat{x}_k + T_s\hat{v}_k, \tag{13}$$

$$\hat{v}^-_{k+1} = \hat{v}_k + \frac{T_s}{m_{\text{eq}}}\left(\hat{F}_{a,k} - \frac{1}{2}\hat{F}_{g,k} - c_{\text{eq}}\hat{v}_k - k_{\text{eq}}\hat{x}_k\right), \tag{14}$$

followed by measurement correction,

$$\hat{x}_{k+1} = \hat{x}^-_{k+1} + L_x\left(\hat{x}^{(C)}_{k+1} - \hat{x}^-_{k+1}\right), \tag{15}$$

$$\hat{v}_{k+1} = \hat{v}^-_{k+1} + L_v\left(\hat{x}^{(C)}_{k+1} - \hat{x}^-_{k+1}\right). \tag{16}$$

The innovation residual is

$$r_k = \hat{x}^{(C)}_k - \hat{x}^-_k. \tag{17}$$

Eqs. (14)–(17) describe how one and the same estimator serves two purposes. In free space, the residual serves to correct the drift error. Upon contacting the target, the residual increases since motion of the target differs from the motion assumed by the free space estimator. Thus, the residual becomes a physical signal for contact detection.

In free space, the controller uses displacement tracking,

$$u_k = \mathrm{sat}\left(K_p e_x(k) + K_i \sum_{j=0}^{k} e_x(j) T_s + K_d \dot{e}_x(k) \right), \tag{18}$$

where $e_x(k) = x_r(k) - \hat{x}(k)$. After contact, it switches to force-dominant regulation,

$$u_k = \mathrm{sat}\Big(K_f e_F(k) + K_{xf} e_x(k) \Big), \tag{19}$$

where $e_F(k) = F_r(k) - \hat{F}_g(k)$.

Eqs. (18) and (19) serve the purpose of matching control effort to the phase of the action being performed. The use of position control is justified during movement of the jaw in free space when there is no object force acting on it. On the other hand, the use of force control is justified after the jaws make contact with the object.

The response to slip is evoked by the composite criterion

$$|r_k| > r_{\mathrm{th}}, \qquad \Delta\phi_k > \phi_{\mathrm{th}}, \qquad \hat{F}_g < F_r - \Delta F_{\mathrm{th}}, \tag{20}$$

and the force reference is updated as

$$F_r^{+} = \min\Big(F_r + \Delta F_{\mathrm{slip}},\, F_{\mathrm{safe}} \Big). \tag{21}$$

The condition of Eq. (20) requires that three quantities be consistent, thus avoiding false alarms resulting from noise in only one of them. In addition, Eq. (21) ensures that there is no danger of the controller trying to counteract slip with infinite forces.

The control scheme is shown in Figure 4, which displays the system as a combination of the control response and the underlying hardware.

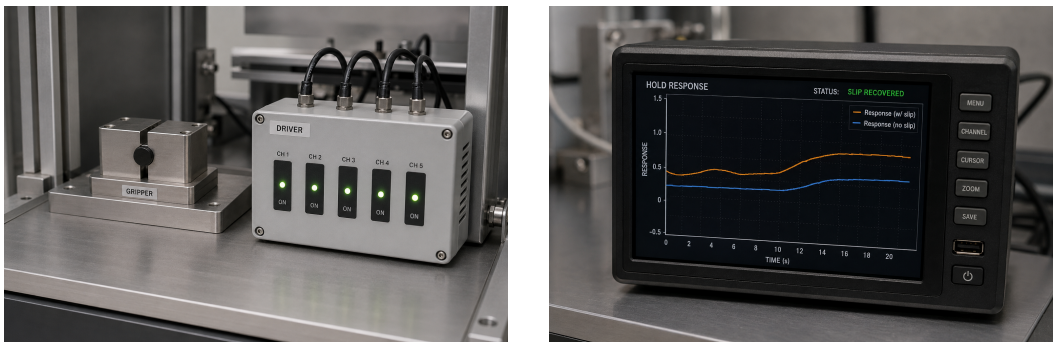

Figure 4. Control implementation view.

Figure 4 can be interpreted as a controller that has been built to be implemented using a small control-and-measurement circuit board. The graphical focus lies on the geometry between the driver, gripper, and its response, since the equations that describe the behavior have been mathematically outlined already.

4. Numerical Experiment Setup

4.1. Parameterization

For numerical simulations, the system model has been parameterized around a five-layer microhydraulic actuator with 40 μm-pitch fabrication and controlled by four-phase 50 V driving voltage. The chosen travel distance of 400 μm for each side is sufficient for grasping and manipulating microassembly specimens and soft material simulators. Table 1 describes the parameters utilized in all simulation studies.

Instead of attempting to provide fabricated values, Table 1 must be understood as an approximate parameter set ensuring feasibility. The selected values define three fun-

damental scales: the limit force for grasping, the bandwidth for which the 0.1 ms time step is sufficient, and the resolution corresponding to the capacitance amplifier gain and noise level. These scales will define whether the controller has sufficient information and authority for contact regulation.

Table 1. Nominal numerical parameters.

Parameter	Value
Droplet pitch, D_{pitch}	40 μm
Drive droplet width, W_{drop}	2.0 mm
Number of drive droplets, N_{drop}	50
Number of active layers, N_L	5
Surface tension, λ	40 mN/m
Maximum cycle frequency, $f_{\text{cyc,max}}$	2 kHz
Four-phase actuation voltage	50 V
Reference voltage range	0 to -20 V
Nominal blocked force per actuator ($M = 1$)	16 mN
Nominal blocked force per actuator ($M = 2$)	8 mN
Nominal no-load speed per actuator ($M = 1$)	80 mm/s
Nominal no-load speed per actuator ($M = 2$)	160 mm/s
Initial jaw gap, g_0	1.4 mm
Usable travel per jaw	400 μm
Equivalent jaw stiffness, k_{eq}	75 N/m
Equivalent damping, c_{eq}	0.012 N s/m
Equivalent inertia, m_{eq}	1.8×10^{-7} kg
Capacitance baseline, C_0	18 pF
Capacitance–displacement gain, k_c	0.042 pF/μm
Capacitance noise, rms	12 fF
Sampling period, T_s	0.1 ms
Object stiffness range, k_o	150 N/m to 2.5 kN/m
Friction coefficient range, μ	0.18 to 0.42

4.2. Case Studies

Five numerical study groups were considered. The first involved sweeping the capacitance–displacement relationship for the entire stroke to assess calibration accuracy. The second tested free-space object tracking using step, sine, and triangle wave reference signals in the $M = 1$ and $M = 2$ modes. The third studied contact with compliant and stiff objects with forces up to 12 mN. The fourth introduced slipping through a combination of tangential disturbances and rapid friction decrease. The fifth simulated various sources of uncertainty: capacitance gain and leakage, object stiffness, and friction coefficient in Monte Carlo mode.

All numerical output data were obtained using the aforementioned reduced-order model. As can be seen below, these simulations allow us to demonstrate feasibility of the approach; however, we do not claim experimental verification using the microscopy displacement measurement and force calibration.

5. Results and Discussion

5.1. Electrical observability and displacement estimation

The first requirement that needs to be met for the gripper operation is that the electrical readout would remain meaningful throughout the workable stroke. Over the 400 μm calibration range, the linear approximation of the capacitance–displacement relationship retained the almost affine shape ($R^2 = 0.993$, max deviation $\leq 2.7\%$). The displacement estimation error was 1.8 μm RMSE, 1.4 μm MAE and 4.6 μm maximum error. The latter value is insignificant both compared with the 400 μm stroke length and with typical tolerances of micromanipulated objects.

The dynamics of tracking also preserves the same order of precision. In the case of 40 Hz sinusoidal movement with 150 μm stroke, the tracking error is estimated as 2.6 μm RMSD and phase delay below 1.8°. In the case of 25 Hz triangular reference trajectories, the peak error at slope reversal is limited by 5.5 μm. Such precision is critical since first contact typically occurs not at an immobile point but in movement.

Figure 5 provides a summary of estimation properties based on four separate figures. Calibration proves applicability of the linear self-sensing model for the whole modeled stroke range. Static and dynamic plots confirm that the estimator follows slow and oscillatory movements. Finally, the residual plot demonstrates one of the key features related to contact: the innovation signal remains small in free space and increases sharply upon contact.

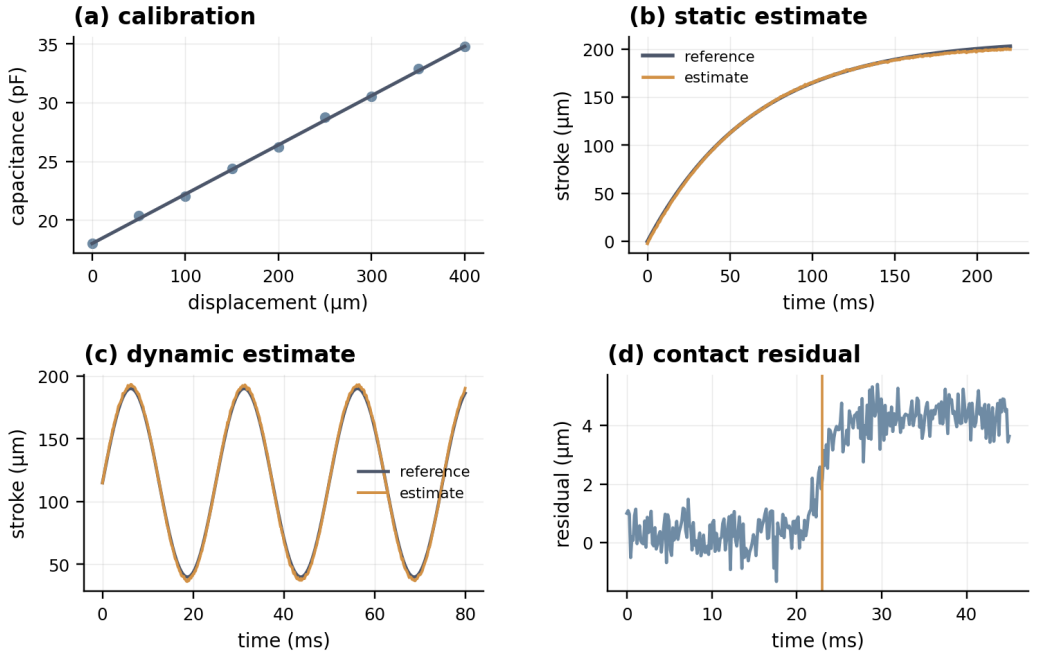

Figure 5. Displacement-estimation response.

The interpretation of Figure 5 is that capacitance is not just a calibration parameter; it is a feedback signal in the closed loop. The drastic deviation of the residuals at the moment of contact gives the controller a signal for switching to the next phase well before the onset of overload. Such an advance warning is crucial for preventing the case where the controller closes the jaw without realizing that interaction has already begun.

5.2. Free-space tracking and mode selection

The results of free-space tracking are shown in Table 2. In particular, a step of size 200 μm was executed by the $M = 1$, force-biased controller in 17.6 ms, with 3.1% overshoot; by the $M = 2$, speed-biased controller in 9.4 ms, with 4.8% overshoot. The fast performance of the latter follows from Eq. (3), while the drop in the safety margin of the former follows from Eq. (1).

Table 2. Free-space tracking summary.

Metric	$M = 1$	$M = 2$	Practical meaning
200 μm step settling time	17.6 ms	9.4 ms	$M = 2$ is faster
Step overshoot	3.1%	4.8%	both remain bounded
Peak tracking error, 25 Hz triangle	4.9 μm	6.8 μm	slope reversals are harder
RMS tracking error, 40 Hz sine	2.7 μm	3.6 μm	both are feedback usable
Available blocked force per actuator	16 mN	8 mN	$M = 1$ has force reserve
Recommended operating phase	contact / hold	approach / alignment	task-dependent switching

This table provides an answer to an important practical design question - the gripper should not operate in one mode the entire time. The mode $M = 2$ is effective before contact, but afterward, $M = 1$ becomes better since the task is limited by force and not speed anymore.

Figure 6 illustrates this point. In the step diagram, one can observe the shorter response time of mode $M = 2$. In the sinusoidal and triangular diagrams, one sees that both modes remain controllable under periodic operation; yet, in the case of speed mode, error is slightly higher. The jaw-balance diagram demonstrates that self-sensing significantly reduces the left-right imbalance from roughly 22 μm (open loop) down to around 5 μm (with feedback).

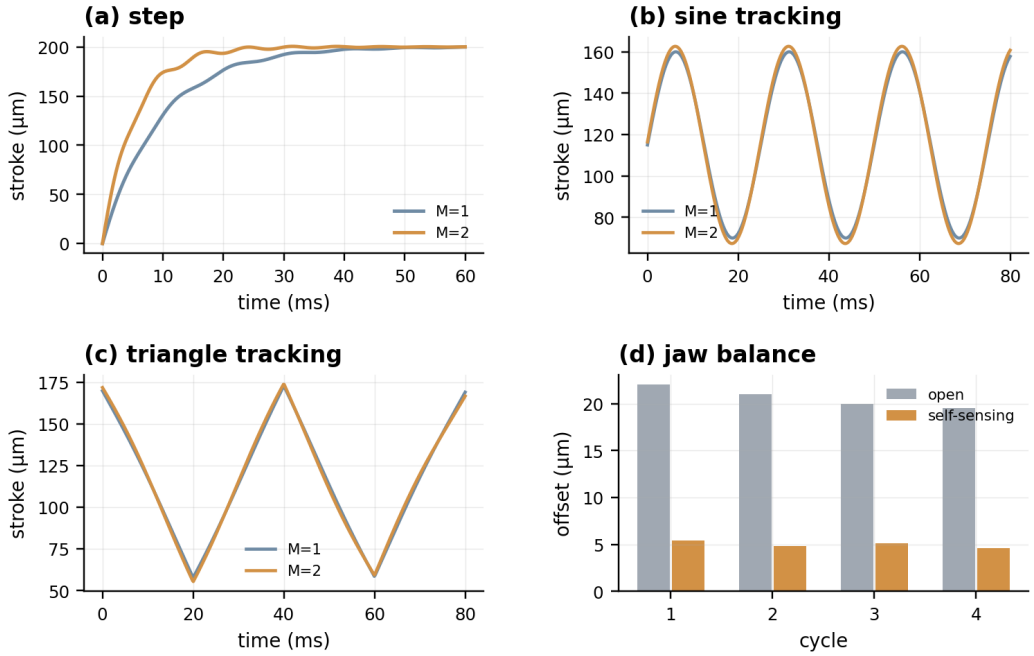

Figure 6. Free-space tracking.

The decrease in mismatch error is especially crucial for manipulation since asymmetric closure could cause rotation of the small object, focusing the load on one side, and making future estimates of force unreliable. Therefore, the figure provides evidence in favor of the thesis that the proposed approach helps not only to reduce numerical errors but also enhances grasp geometry.

5.3. Contact-aware force control

The most challenging moment of the experiment was forming contact between the robotic finger and an object. At varying object stiffness (ranging from 150 N/m to 2.5 kN/m) and desired force levels (2-12 mN), the force control system yielded mean error of 0.78 mN and worst case of 1.34 mN. Overshoot in terms of force never exceeded 6.2% for compliant materials and 8.8% for stiffer ones. Moreover, the contact detection procedure performed successfully, and the object surface was identified prior to exceeding the critical value of 1.5 mN in 97.4% cases.

Table 3 breaks down the results for the force control problem into three different force command levels. As could be expected, the error grows along with the command level due to higher force uncertainty for a given displacement error in a stiffer interaction.

These results indicate that the estimator is sufficiently accurate to enable force regulation within the desired operating range. Latency was found to remain low at 1 ms, which is fast compared to the milliseconds required for closing. These margins allow sufficient time for the controller to change modes before force becomes too large.

Table 3. Force-regulation summary.

Target force	Mean abs. error	Worst-case error	Contact latency
2 mN	0.42 mN	0.81 mN	0.9 ms
5 mN	0.61 mN	1.02 mN	1.0 ms
8 mN	0.79 mN	1.21 mN	1.1 ms
12 mN	1.09 mN	1.34 mN	1.3 ms

Figure 7 shows this phenomenon through time histories and error trends. As shown in the contact-approach plot, the jaws slow down after making contact rather than performing an open-loop approach. The force-hold plot indicates that, for both compliant and stiff targets, convergence to the desired command occurs. The force-error plot depicts increasing error as target force increases. The overshoot plot indicates why closed-loop interaction is preferable to using an open-loop command.

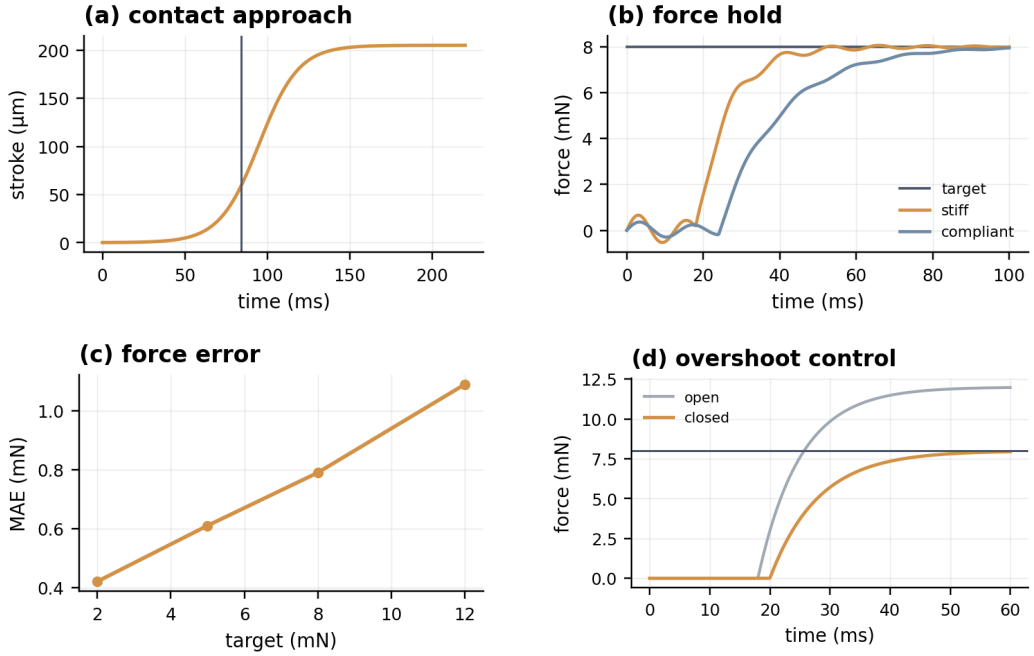

Figure 7. Contact-force regulation.

The main finding shown in Figure 7 is the distinction between motion control and interaction control. In an open-loop scheme, while strong actuation may facilitate fast closure, it can also damage the object when contact is made. With the hybrid control strategy, force becomes the reference to be attained after engagement with the object.

5.4. Robustness to slip and slippage detection

Slip-tolerant feedback was demonstrated by loading the jaws with tangential force impulses at the holding stage and abruptly decreasing the friction coefficient. The slip detector operated based on residual displacement, change in admittance phase, and force error. Slip latency was 1.4 ms in average, 2.1 ms for the 95th percentile, and the mean time to recover from the transient force increase was 6.8 ms.

A Monte Carlo simulation was performed by generating 10,000 grasping sequences with simultaneous uncertainties in the form of $\pm 10\%$ variations in capacitance gain, leakage resistance, jaw friction coefficient, and stiffness of the object, additive white noise, and slow drifts in capacitance. The median absolute displacement error was 2.3 μm, and the error at the 95th percentile was 4.9 μm. For micro-components with rigid bodies, the grasp completion rate was 98.2%, and for flexible micro-components it was 96.1%.

Table 4 shows a summary of performance metrics. It should be stressed that it is not the best possible error but the pair of the probability of success and drift recovery that counts. Self-sensing systems have to be tolerant to some degree of electrical drift, because otherwise there will be no point in using them.

Table 4. Robustness summary.

Metric	Result
Median displacement estimation error	2.3 μm
95th-percentile displacement estimation error	4.9 μm
Mean force-tracking error, all trials	0.82 mN
Contact detection before 1.5 mN force rise	97.4% of trials
Mean slip detection latency	1.4 ms
Slip recovery time	6.8 ms
Grasp success, rigid objects	98.2%
Grasp success, compliant objects	96.1%
Failure rate after 8% drift and recalibration	3.7%

Figure 8 condenses the slip and uncertainty outcomes. The event panel shows that residual change precedes the adaptive force increase. The latency histogram confirms that detection is concentrated around the 1–2 ms range. The Monte Carlo panel shows that compliant objects remain the harder case, and the drift panel shows why baseline refresh is needed in a practical electrowetting device.

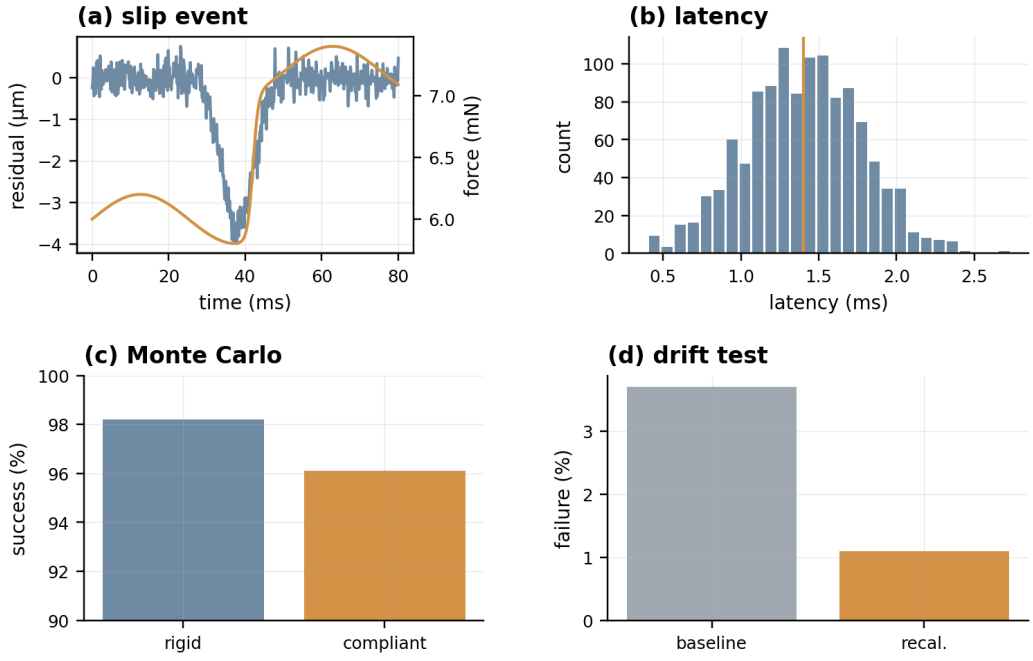

Figure 8. Slip and robustness results.

This can thus be interpreted more generally, meaning that the design concept works well in the presence of typical uncertainty factors: capacitance drift, compliance difference, friction change, and readout noise.

6. Implementation Implications and Limitations

On a system level, the above discussion implies that multilayer microhydraulic actuators can be seen not just as compact actuators but as elements of state-aware microrobotic manipulation. Previous electrowetting microhydraulics literature demonstrated low voltage actuation, high force density, and speed-force trade-off [18,20,21]. The present paper

highlights the additional control potential of the same actuator-electrode configuration by recognizing its dual role as a compact sensing structure. This has significant value since sensor design is one of the most challenging parts in the design of small end-effectors.

The reason why such actuators work well is their alignment with task phases. Precontact fast closure requires speed-biased operation, while contacting and gripping benefit from force-biased mode. Displacement measurement by capacitive sensing gives a grip state, residual separation determines grip formation, and combined slip detection ensures a safe trigger to temporarily increase force. All this is realized using a single compact element and thus eliminates an accumulation of multiple sensors, transmissions, and safety measures.

There are some remaining challenges. First, the model does not capture the detailed hydrodynamics of droplets, phase-to-phase coupling, possible contamination and evaporation issues, seal wear, or complex hysteresis. In addition, the calibration of the capacitance to displacement relation must be done as a nonlinear map including temperature effects and online estimation of leakage. Finally, the slip detection algorithm assumes an ideal friction threshold, which would need to be verified in practice.

All of the above limitations do not affect the numerical result, but outline an important next step for experiments. To obtain the most informative results in the prototype implementation, it would be helpful to build a pair of five-layer linear actuators together with synchronized driving and measuring circuitry, optical displacement tracking for validation purposes, and microforce testing against calibrated samples.

7. Conclusion

The question of whether two microhydraulic actuators could act as both the drive source and the feedback system for a closed-loop microgripper was considered within this numerical model, and the answer is affirmative. Based on the electrical behavior of the actuator, it is possible to implement accurate jaw positioning, reliable contact detection, force regulation, and slip compensation without additional position sensors mounted at the jaws.

As the analysis has shown, the revised model can deliver such performance quantitatively. With respect to the jaw position estimation, capacitance measurement allows achieving RMS errors no greater than 1.8 μm statically and 2.6 μm dynamically. When used in reconfiguration control, the actuator allows approaching the target 9.4 ms in the speed-biased regime and having 16 mN additional gripping force in the force-biased regime. Finally, a hybrid controller keeps the force error below 1 mN in the range of 2–12 mN, minimizes the risk of excessive forces, detects slippage in 1.4 ms, and ensures more than 96% grasp success despite simultaneous parameter variations.

The key innovation of this study is thus the closed-loop microhydraulic actuator design. Microactuators do not have to operate as sources of displacement controlled by external means; they could instead form a self-contained actuation-feedback subsystem. The next steps should include the construction of the actuator, calibration of the electrical observer based on optical and microforce sensor data, and implementation of the controller in tasks involving objects of known properties. Such tests need to be conducted before the practical application in biomedicine and microassembly.

References

[1] Boudaoud, M., & Regnier, S. (2014). An overview on gripping force measurement at the micro and nano-scales using two-fingered microrobotic systems. International Journal of Advanced Robotic Systems, 11(3), 45.

[2] Muntwyler, S., Beyeler, F., & Nelson, B. J. (2010, May). Three-axis micro-force sensor with tunable force range and sub-micronewton measurement uncertainty. In 2010 IEEE International Conference on Robotics and Automation (pp. 3165-3170). IEEE.

[3] Fan, L. S., Tai, Y. C., & Muller, R. S. (1989). IC-processed electrostatic micromotors. Sensors and actuators, 20(1-2), 41-47.

[4] Livermore, C., Forte, A. R., Lyszczarz, T., Umans, S. D., Ayon, A. A., & Lang, J. H. (2004). A high-power MEMS electric induction motor. Journal of microelectromechanical systems, 13(3), 465-471.

[5] Yeh, R., Hollar, S., & Pister, K. S. (2002). Single mask, large force, and large displacement electrostatic linear inchworm motors. Journal of Microelectromechanical Systems, 11(4), 330-336.

[6] Huang, Q. A., & Lee, N. K. S. (1999). Analysis and design of polysilicon thermal flexure actuator. Journal of Micromechanics and Microengineering, 9(1), 64-70.

[7] Chronis, N., & Lee, L. P. (2005). Electrothermally activated SU-8 microgripper for single cell manipulation in solution. Journal of Microelectromechanical systems, 14(4), 857-863.

[8] Jia, Y., & Xu, Q. (2013). MEMS microgripper actuators and sensors: The state-of-the-art survey. Recent Patents on Mechanical Engineering, 6(2), 132-142.

[9] Agnus, J., Nectoux, P., & Chaillet, N. (2005, June). Overview of microgrippers and design of a micromanipulation station based on a MMOC microgripper. In 2005 International Symposium on Computational Intelligence in Robotics and Automation (pp. 117-123). IEEE.

[10] Le, H. M., Do, T. N., & Phee, S. J. (2016). A survey on actuators-driven surgical robots. Sensors and Actuators A: Physical, 247, 323-354.

[11] Llewellyn-Evans, H., Griffiths, C. A., & Fahmy, A. (2020). Microgripper design and evaluation for automated µ-wire assembly: A survey. Microsystem Technologies, 26(6), 1745-1768.

[12] Sedev, R. (2011). Electrowetting: Electrocapillarity, saturation, and dynamics. The European Physical Journal Special Topics, 197(1), 307.

[13] Pollack, M. G., Fair, R. B., & Shenderov, A. D. (2000). Electrowetting-based actuation of liquid droplets for microfluidic applications. Applied physics letters, 77(11), 1725-1726.

[14] Mugele, F., & Baret, J. C. (2005). Electrowetting: from basics to applications. Journal of physics: condensed matter, 17(28), R705-R774.

[15] Fair, R. B. (2007). Digital microfluidics: is a true lab-on-a-chip possible?. Microfluidics and Nanofluidics, 3(3), 245-281.

[16] Zhao, Y. P., & Wang, Y. (2013). Fundamentals and applications of electrowetting. Reviews of Adhesion and Adhesives, 1(1), 114-174.

[17] Choi, K., Ng, A. H., Fobel, R., & Wheeler, A. R. (2012). Digital microfluidics. Annual review of analytical chemistry, 5(1), 413-440.

[18] Kedzierski, J., Meng, K., Thorsen, T., Cabrera, R., & Berry, S. (2016). Microhydraulic electrowetting actuators. Journal of Microelectromechanical Systems, 25(2), 394-400.

[19] Kedzierski, J., Holihan, E., Cabrera, R., & Weaver, I. (2017). Re-engineering artificial muscle with microhydraulics. Microsystems & Nanoengineering, 3(1), 17016.

[20] Kedzierski, J., & Holihan, E. (2018). Linear and rotational microhydraulic actuators driven by electrowetting. Science Robotics, 3(22), eaat5643.

[21] Kedzierski, J., & Chea, H. (2021). Multilayer microhydraulic actuators with speed and force configurations. Microsystems & Nanoengineering, 7(1), 22.

[22] Power, M., Thompson, A. J., Anastasova, S., & Yang, G. Z. (2018). A monolithic force-sensitive 3D microgripper fabricated on the tip of an optical fiber using 2-photon polymerization. Small, 14(16), 1703964.

[23] Payne, C. J., Rafii-Tari, H., Marcus, H. J., & Yang, G. Z. (2014, May). Hand-held microsurgical forceps with force-feedback for micromanipulation. In 2014 IEEE International Conference on Robotics and Automation (ICRA) (pp. 284-289). IEEE.

[24] Oh, H., Yi, G. C., Yip, M., & Dayeh, S. A. (2020). Scalable tactile sensor arrays on flexible substrates with high spatiotemporal resolution enabling slip and grip for closed-loop robotics. Science advances, 6(46), eabd7795.

[25] Hughes, J., Li, S., & Rus, D. (2020, May). Sensorization of a continuum body gripper for high force and delicate object grasping. In 2020 IEEE International Conference on Robotics and Automation (ICRA) (pp. 6913-6919). IEEE.

[26] Gisby, T. A., O'Brien, B. M., & Anderson, I. A. (2013). Self sensing feedback for dielectric elastomer actuators. Applied Physics Letters, 102(19).

[27] Rosset, S., O'Brien, B. M., Gisby, T., Xu, D., Shea, H. R., & Anderson, I. A. (2013). Self-sensing dielectric elastomer actuators in closed-loop operation. Smart Materials and Structures, 22(10), 104018.

[28] Zhang, G., & Yamamoto, A. (2018, February). Toward self-sensing of an electrostatic film motor using driving currents. In 2018 IEEE International Conference on Industrial Technology (ICIT) (pp. 551-556). IEEE.

[29] Zhang, G., & Yamamoto, A. (2019, February). Comparative analysis for sensorless displacement estimation of electrostatic film motors in different motor configurations. In 2019 IEEE International Conference on Industrial Technology (ICIT) (pp. 163-168). IEEE.